MNRAS 000, 1–11 (2021) Preprint 31 July 2022 Compiled using MNRAS LATEX style file v3.0

A prescription for the asteroseismic surface correction

Yaguang Li (李亚光) [1,2] ⋆ Timothy R. Bedding [1,2] † Dennis Stello [3] Daniel Huber [4] Marc Hon [4], Meridith Joyce [5] Tanda Li (李坦达) [6] Jean Perkins [7] Timothy R. White [1,2], Joel C. Zinn [8] Andrew W. Howard [9] and Howard Isaacson [10]

[1] *Sydney Institute for Astronomy (SIfA), School of Physics, University of Sydney, NSW 2006, Australia*
[2] *Stellar Astrophysics Centre, Department of Physics and Astronomy, Aarhus University, Ny Munkegade 120, DK-8000 Aarhus C, Denmark*
[3] *School of Physics, University of New South Wales, 2052, Australia*
[4] *Institute for Astronomy, University of Hawai'i, 2680 Woodlawn Drive, Honolulu, HI 96822, USA*
[5] *Space Telescope Science Institute, 3700 San Martin Dr, Baltimore, MD 21218, USA*
[6] *Department of Astronomy, Beijing Normal University, Haidian District, Beijng 100875, China*
[7] *Monterey Institute for Research in Astronomy, 200 8th St, Marina, CA 93933*
[8] *Department of Astrophysics, American Museum of Natural History, Central Park West at 79th Street, New York, NY 10024, USA*
[9] *Division of Physics, Mathematics and Astronomy, Caltech, 1200 E California Blvd, Pasadena CA 91125, USA*
[10] *Department of Astronomy, University of California at Berkeley, 501 Campbell Hall, Berkeley, CA 94720-3411, USA*

Accepted XXX. Received YYY; in original form ZZZ

ABSTRACT

In asteroseismology, the surface effect is a disparity between the observed and the modelled oscillation frequencies. It originates from improper modelling of the surface layers in stars with solar-like oscillations. Correcting the surface effect usually requires using functions with free parameters, which are conventionally fitted to the observed frequencies. On the basis that the correction should vary smoothly across the H–R diagram, we parameterize it as a simple function of three stellar surface properties: surface gravity, effective temperature, and metallicity. We determine this function by fitting stars ranging from main-sequence dwarfs to red-giant-branch stars. The absolute amount of the surface correction increases with surface gravity, but the ratio between it and $\nu_{\rm max}$ decreases. Applying the prescription has an advantage of eliminating unrealistic surface correction, which improves parameter estimations with stellar modelling. Using two open clusters, we found that adopting the prescription can help reduce the scatter of the model-derived ages for each star in the same cluster. For an application, we provide a new revision for the $\Delta\nu$ scaling relation, using our prescription to account for the surface effect in models. The values of the correction factor, $f_{\Delta\nu}$, are up to 2% smaller than those determined without the surface effect considered, suggesting decreases of up to 4% in asteroseismic scaling radii and up to 8% in asteroseismic scaling masses. This revision brings the asteroseismic properties into agreement with those determined from eclipsing binaries. Finally, the new correction factor and the stellar models with the corrected frequencies are made publicly available.

Key words: stars: solar-type – stars: oscillations (including pulsations) – stars: low-mass

1 INTRODUCTION

Correcting the asteroseismic surface effect has so far been a troublesome procedure. As summarised by Houdek et al. (2017), convection affects pulsation properties through turbulent pressure, opacity variations, and convective energy flux. In addition, Li et al. (2021) suggested that layers formed by small-scale magnetic fields could reflect p-mode oscillations. All these processes are poorly modelled in the near-surface convective atmosphere in most 1D stellar models (Christensen-Dalsgaard et al. 1988; Dziembowski et al. 1988). Improvements have been seen with the surface layers replaced by 3D averaged atmospheric models, producing more realistic equilibrium structures (Rosenthal et al. 1999; Magic & Weiss 2016; Jørgensen et al. 2017; Trampedach et al. 2017; Jørgensen et al. 2018, 2019; Mosumgaard et al. 2020), or with time-dependent 1D convection models, accounting for the coupling between oscillation and convection (Balmforth 1992; Grigahcène et al. 2012; Christensen-Dalsgaard 2012; Houdek et al. 2017, 2019; Belkacem et al. 2021; Philidet et al. 2021).

In practice, the surface effect is usually corrected empirically with simple functions of frequency. Christensen-

⋆ yaguang.li@sydney.edu.au
† tim.bedding@sydney.edu.au

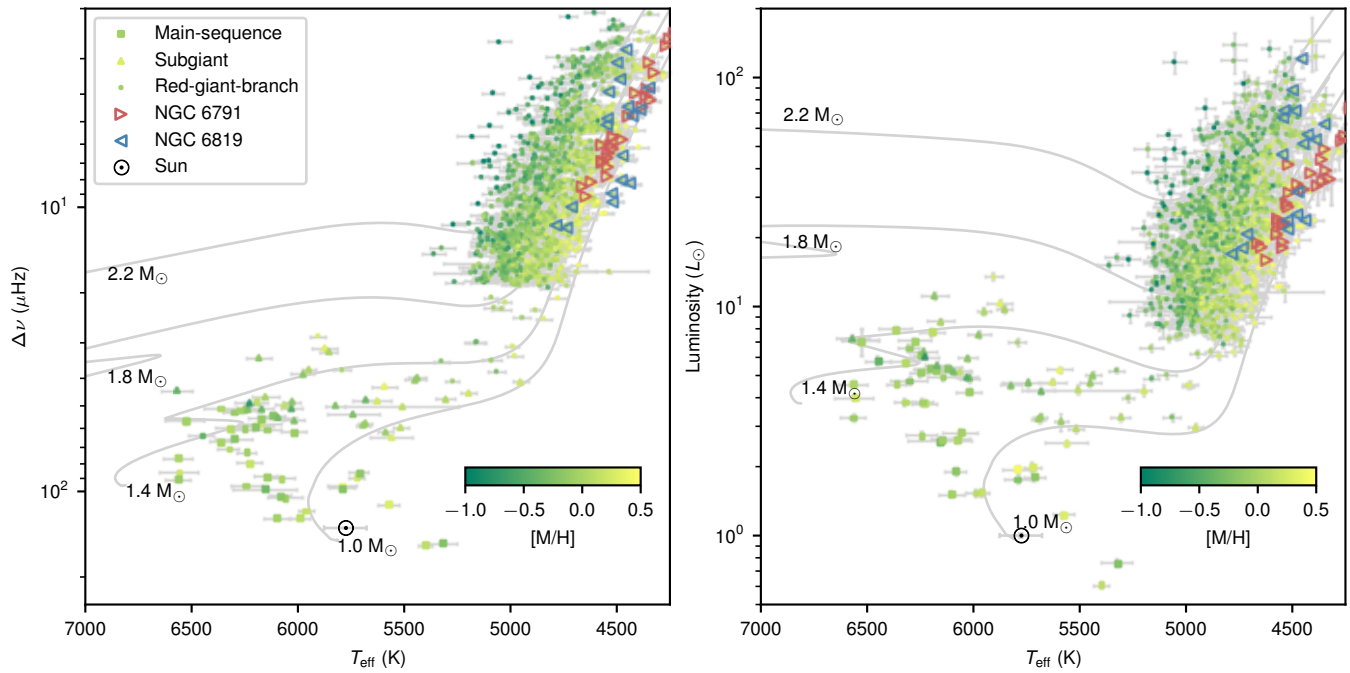

Figure 1. Evolutionary diagrams of the studied sample in this work. Left: $\Delta\nu$ versus $T_{\rm eff}$. Right: *Gaia* luminosity versus $T_{\rm eff}$. The $M = 1.0,\ 1.4,\ 1.8$ and $2.2\ {\rm M}_\odot$ evolutionary tracks are shown in grey lines.

Dalsgaard et al. (1989) provided a justification, based on a perturbation to an asymptotic formalism of acoustic modes. By rescaling the frequency correction obtained from the solar standard model, Silva Aguirre et al. (2015) and Houdek et al. (2019) applied it to other main-sequence stars. Several other correction formula were also put forward (e.g. Kjeldsen et al. 2008; Sonoi et al. 2015). In particular, Gough (1990) suggested that the corrections are proportional to the cubic and the inverse of frequencies scaled by mode inertia:

$$\delta\nu = \left[a_3(\nu/\nu_{\rm max})^3 + a_{-1}(\nu/\nu_{\rm max})^{-1}\right]/I, \quad (1)$$

where a_3 and a_{-1} are the free parameters to be determined. The frequency of maximum power, $\nu_{\rm max}$, is evaluated via the scaling relation (Brown et al. 1991; Kjeldsen & Bedding 1995):

$$\frac{\nu_{\rm max}}{\nu_{\rm max,\odot}} \approx \frac{g}{g_\odot}\left(\frac{T_{\rm eff}}{T_{\rm eff,\odot}}\right)^{-1/2}, \quad (2)$$

where we adopt $g_\odot = 274$ m/s^2, $T_{\rm eff,\odot} = 5777$ K, and $\nu_{\rm max,\odot} = 3090\ \mu$Hz throughout this work. Since the cubic term usually dominates the frequency correction, another correction form is written as

$$\delta\nu = a_3(\nu/\nu_{\rm max})^3/I, \quad (3)$$

where a_3 is the free parameter.

These two functional forms have shown excellent performance. Ball & Gizon (2014, 2017) showed that they work well for radial modes on the Sun and red-giant-branch stars, albeit with some caveats for mixed modes (Ong et al. 2021a,b). Many works concluded the inverse-cubic form could obtain an overall good fit (Schmitt & Basu 2015; Compton et al. 2018; Nsamba et al. 2018; Jørgensen et al. 2020) and correctly recover the dynamical stellar properties of binary systems (Jørgensen et al. 2020).

The correction usually works as follows. Given a star with a set of observational frequencies and a stellar model with a set of theoretical frequencies, one can calculate the difference between the two frequency sets. This difference is then fitted to the right-hand-side of the frequency correction function (Eq. 1 or 3) to determine the free parameters. The amount of frequency correction is then calculated with the best-fitted values and added to the theoretical frequencies.

One problem with this method is that the surface correction can only be determined with a fit to observed frequencies. It does not allow us to estimate the surface terms for a theoretical model without observational data. More seriously, it can lead to a model with an unphysically large (or small) surface correction that fits the data well but is a poor representation of the star. In this paper, we tackle this problem through a simple prescription for the surface effect, assuming that it varies smoothly with stellar parameters. This variation is then constrained by an ensemble fit to a wide range of stars (Sections 2 and 3). Adopting this prescription improves parameter estimations with stellar modelling (Section 4). It further enables an improved correction to the commonly-used $\Delta\nu$ scaling relation (Section 5).

2 DATA PREPARATION

2.1 Observational sample

To parameterize the surface correction as a function of stellar properties, we need a sample of stars spanning a sufficiently large parameter space. Our sample (see Fig. 1) consists of stars with measured individual frequencies: the Sun (Broomhall et al. 2009), the SONG subgiant μ Herculis (Grundahl et al. 2017), *Kepler* main-sequence dwarfs (Lund

et al. 2017), *Kepler* subgiants (Li et al. 2020a) and *Kepler* red-giant-branch (RGB) stars with $\Delta\nu > 2$ μHz (Li et al. 2022).

We obtained new high-resolution spectra for 64 stars in our sample using the HIRES spectrograph (Vogt et al. 1994) at the Keck-I 10-m telescope on Maunakea observatory, Hawai'i. The spectra were obtained and reduced as part of the California Planet Search queue (CPS, Howard et al. 2010). We used the C5 decker and obtained spectra with a S/N per pixel of 80 at ~ 600 nm with a spectral resolving power of $R \sim 60000$. To measure metallicities [M/H], we applied Specmatch-synth (Petigura 2015), which fits a synthetic grid of model atmospheres and has been extensively validated through the California Kepler Survey (Petigura et al. 2017; Johnson et al. 2017). For those stars without HIRES spectra, we compiled metallicities from various sources, including APOGEE DR16 (Ahumada et al. 2020) and TRES spectra from Lund et al. (2017) (listed in the order of priority) wherever possible. All measurements were brought to the APOGEE abundance scale by adding constant offsets, determined with the [M/H] measurements of same stars. Because of the limited number of metal-poor stars, we restricted our sample to have [M/H] > -0.8 dex.

We determined the effective temperatures, $T_{\rm eff}$, with *Gaia* and 2MASS photometry, using the infrared flux method (IRFM) calibrated by Casagrande et al. (2021). This $T_{\rm eff}$ scale was benchmarked against solar twins, Gaia benchmark stars, and interferometry.

We determined luminosities, L, using *Gaia* DR3 (Gaia Collaboration et al. 2016, 2021). *Gaia* parallaxes are known to have zero-point offsets, which we corrected using a model from Lindegren et al. (2021). The reported parallaxes also have underestimated uncertainties. Therefore we inflated them by a factor of 1.3, according to external calibrations (El-Badry et al. 2021; Zinn 2021; Maíz Apellániz et al. 2021). We then calculated the luminosities by combining the parallaxes with the 2MASS K-band magnitudes and using the "direct" method in the software ISOCLASSIFY (Huber et al. 2017; Berger et al. 2020), which implements the Green et al. (2019) dust map and the bolometric corrections from MIST models (Choi et al. 2016).

Additionally, we used RGB stars from two *Kepler* clusters as a test sample: NGC 6791 (Basu et al. 2011; McKeever et al. 2019; Brogaard et al. 2021) and NGC 6819 (Stello et al. 2010; Corsaro et al. 2012; Handberg et al. 2017). These cluster stars were not used for fitting the prescription, but for validating the result (Section 4). We estimated their stellar parameters following the same procedure illustrated above. Fig. 1 shows an overview of our sample on the $\Delta\nu$–$T_{\rm eff}$ and H–R diagrams.

2.2 Stellar models

We calculated a grid of stellar models using Modules for Experiments in Stellar Astrophysics (MESA, version r15140; Paxton et al. 2011, 2013, 2015, 2018, 2019) to model stellar evolution and structure, and GYRE (version 6.0.1; Townsend & Teitler 2013) to calculate adiabatic frequencies from the structure profiles computed from MESA.

Here, we summarise the input physics for the constructed models. We used the Henyey et al. (1965) description of the mixing length theory to formulate convection, with the mixing length being one of the free parameters, since a solar-calibrated mixing length can not fit stars with various stellar properties (Tayar et al. 2017; Joyce & Chaboyer 2018). We set the convective overshoot with an exponential scheme discussed by Herwig (2000). For core overshoot, we set the efficiency parameter $f_{\rm ov,core}$ as a function of mass, according to the calibration from eclipsing binaries (equation 2 of Claret & Torres 2018). For envelope overshoot, we set $f_{\rm ov,env}$ as 0.006, according to a solar calibration with our adopted input physics.

We chose the current solar photospheric abundance as the reference scale for metallicity: $X_\odot = 0.7381$, $Y_\odot = 0.2485$, $Z_\odot = 0.0134$ (Asplund et al. 2009, the AGSS09 scale). Hence the metallicity is

$$[\mathrm{M/H}] = \log_{10}(Z/X) - \log_{10}(Z_\odot/X_\odot). \quad (4)$$

The opacity tables were accordingly chosen based on the AGSS09 metal mixture. MESA implements electron conduction opacities (Cassisi et al. 2007) and radiative opacities from OPAL (Iglesias & Rogers 1993, 1996), except low-temperature data (Ferguson et al. 2005) and the high-temperature Compton-scattering regime (Buchler & Yueh 1976). The equation of state adopted by MESA blends from OPAL (Rogers & Nayfonov 2002), SCVH (Saumon et al. 1995), PTEH (Pols et al. 1995), HELM (Timmes & Swesty 2000), and PC (Potekhin & Chabrier 2010). We adopted nuclear reaction rates from JINA REACLIB database. We only considered a minimal set of elements specified in `basic.net` of MESA. We did not account for atomic diffusion or gravitational settling in the models.

For the surface boundary conditions, we used the grey model atmosphere together with Eddington T–τ integration (Eddington 1926). We caution that by default, MESA does not include the atmosphere in the output structure. The resulting bias looks very similar to the surface effect, although the amount of correction is larger. To avoid this, one should specifically set `add_atmosphere_to_pulse_data` as `.true.`

The free parameters for the model grid are stellar mass $M \in (0.8, 1.8)$ $M_\odot$, initial helium abundance $Y_{\rm init} \in (0.22, 0.32)$, metallicity [M/H] $\in (-1.0, 0.5)$ (the corresponding $Z_{\rm init}$ ranges from 0.0012 to 0.042), and mixing-length parameter $\alpha_{\rm MLT} \in (1.3, 2.8)$. These four parameters were uniformly sampled in a quasi-random Sobol sequence with a total number of 8191 (Bellinger et al. 2016). Each set of parameters uniquely determines an evolutionary track. Along each evolutionary track, we saved one structure model at least every 0.3 μHz in $\Delta\nu$ or 5 K in $T_{\rm eff}$. For each structure model, we calculated radial mode frequencies with GYRE within $\nu_{\rm max} \pm 5w$, where $w = \exp(0.964 \ln \nu_{\rm max} - 1.715)$, a frequency range expected to show solar-like oscillations (Lund et al. 2017; Yu et al. 2018; Kim & Chang 2021). We used the 6th-order Gauss-Legendre Magnus method to solve the adiabatic oscillations. We caution that a lower-order algorithm could produce inaccurate frequencies, which differ by an amount larger than the typical observational uncertainties.

3 PRESCRIBING THE SURFACE CORRECTION

3.1 The prescription

Since the surface effect is related to the model atmosphere, it is reasonable to assume it is a smooth function of surface parameters, i.e. $\log g$, $T_{\rm eff}$, and [M/H]. This assumption is

supported by 3D atmospheric simulations (Sonoi et al. 2015; Manchon et al. 2018) and 1D non-adiabatic convection models (Houdek et al. 2019). Those works suggested that the surface correction at $\nu_{\rm max}$, denoted by $\delta\nu_{\rm m}$, varies from star to star as a function of $T_{\rm eff}$ and g. Hence, we propose a prescription for $\delta\nu_{\rm m}$ as follows:

$$\delta\nu_{\rm m} = a \cdot (g/g_\odot)^b \cdot (T_{\rm eff}/T_{\rm eff,\odot})^c \cdot (d \cdot [{\rm M/H}] + 1), \quad (5)$$

where the free parameters to be determined are $\theta_s = \{a, b, c, d\}$. By construction, the parameter a is the amount of surface correction at $\nu_{\rm max}$ for a solar model. If we adopt the cubic formula, for each star we can directly use Eq. 5 to solve the surface term a_3 in Eq. 3 with ν equal to $\nu_{\rm max}$. To obtain the mode inertia I on the RHS of Eq. 3, we interpolated $(\nu/I)^3$ to the frequency $\nu_{\rm max}$.

If we adopt the inverse-cubic formula to correct model frequencies, another equation is needed since there are two surface terms, a_{-1} and a_3. We propose the surface correction at s times of $\nu_{\rm max}$, denoted by $\delta\nu'_{\rm m}$, also varies with the surface parameters:

$$\delta\nu'_m = a' \cdot (g/g_\odot)^{b'} \cdot (T_{\rm eff}/T_{\rm eff,\odot})^{c'} \cdot (d' \cdot [{\rm M/H}] + 1). \quad (6)$$

Together with Eq. 5, the free parameters in this prescription are $\theta_s = \{a, b, c, d, a', b', c', d'\}$. By varying the value of s, we found no obvious changes to the solutions of those free parameters. Hence, we fixed s at 1.1, so that $\delta\nu'_{\rm m}$ represents the amount of surface correction at $1.1\nu_{\rm max}$. For each star, we then used Eq. 5 and Eq. 6 to solve a_{-1} and a_3 in Eq. 1 with $\nu = \nu_{\rm max}$ and $\nu = 1.1\nu_{\rm max}$, respectively. To calculate the RHS of Eq. 1, we interpolated $(\nu/I)^3$ and $(\nu/I)^{-1}$ to the frequency $\nu_{\rm max}$.

3.2 Fitting method

We now describe the fitting method to obtain the surface parameters θ_s in the prescriptions. They determine the amount of surface correction of each model $\theta_m = \{M, Y_{\rm init}, \alpha_{\rm MLT}, [{\rm M/H}], {\rm age}\}$. For each star i, we considered three classical constraints $q = \{L, T_{\rm eff}, [{\rm M/H}]\}$ (e.g. Valle et al. 2015; Duan et al. 2021; Jiang & Gizon 2021):

$$\chi^2_{{\rm classical},i} = \sum_q \frac{(q_{{\rm mod},i} - q_{{\rm obs},i})^2}{\sigma^2_{q,i}}. \quad (7)$$

The seismic constraints include radial mode frequencies, normalised by the number of observed modes N_i (Roxburgh 2016; Aguirre Børsen-Koch et al. 2022):

$$\chi^2_{{\rm seismic},i} = \frac{1}{N_i}\sum_n^{N_i} \frac{(\nu_{{\rm mod},n,i} + \delta\nu_{n,i} - \nu_{{\rm obs},n,i})^2}{\sigma^2_{\rm mod} + \sigma^2_{{\rm obs},n,i}}, \quad (8)$$

where $\delta\nu_{n,i}$ is the amount of surface correction, and $\sigma_{\rm mod}$ is the systematic uncertainty of stellar model frequencies, due to the undersampling of the model grid (Li et al. 2020b; Ong et al. 2021b). To evaluate $\sigma_{\rm mod}$, we identified the best-fitting model (using the above $\chi^2_{\rm seismic}$ and treating $\sigma_{{\rm mod},i}$ as 0) and calculated its root-mean-square difference between the observed and corrected modelled frequencies. At this step, the amount of surface correction for each mode, $\delta\nu_{n,i}$, was determined by fitting Eq. 1 or 3 to the actual differences between the uncorrected model frequencies $\nu_{{\rm mod},n,i}$ and the observed frequencies $\nu_{{\rm obs},n,i}$ (i.e. the traditional star-by-star surface correction). We then fitted the root-mean-square differences as a function of $\nu_{\rm max}$ and $T_{\rm eff}$ for the whole sample and used this function to describe $\sigma_{\rm mod}$, which gave

$$\sigma_{\nu_{\rm mod}}/\mu{\rm Hz} = 1.65 \cdot (\nu_{\rm max}/\nu_{{\rm max},\odot})^{1.45} (T_{\rm eff}/T_{{\rm eff},\odot})^{2.30}. \quad (9)$$

For our final fitting, $\delta\nu_{n,i}$ was calculated using the prescription described in section 3.1. To obtain the probability distributions of the surface parameters, we marginalised the probability over other model parameters.

$$p_i(\theta_s) = \int \exp\left[-\left(\chi^2_{{\rm seismic},i} + \chi^2_{{\rm classical},i}\right)/2\right] \, {\rm d}\theta_m. \quad (10)$$

Finally, putting them together, we maximised the joint probability from all stars in the sample:

$$p(\theta_s) = \prod_i p_i(\theta_s) \quad (11)$$

3.3 Fitting results

In Table 1, we show the best fitted values of the surface parameters in the prescriptions. The inverse-cubic and the cubic models show little differences. Therefore we stick to the inverse-cubic model for discussion in the rest of the paper. To visualise this relation, we colour-coded the values of $\delta\nu_{\rm m}$ and $\delta\nu_{\rm m}/\nu_{\rm max}$ in Fig. 2 on the $\Delta\nu$–$T_{\rm eff}$ diagrams. In terms of the absolute value $\delta\nu_{\rm m}$ (which is always negative), the main-sequence stars have the largest amount of surface correction. It decreases towards higher $T_{\rm eff}$ (hotter F-stars) and smaller $\Delta\nu$ (more luminous red giants). Concerning the relative value of $\delta\nu_{\rm m}$ with respect to $\nu_{\rm max}$, the trend is reversed. The main-sequences stars have smaller correction, and the surface effect becomes increasingly significant for luminous red giants. Those trends are similar compared to those found by Trampedach et al. (2017, Fig. 5 and 6), who improved the mean atmospheric structure with 3D-averaged models (the so-called "structural effect").

Sonoi et al. (2015, Eqs. 9 and 10) also studied the structural effect, mainly for dwarfs and subgiants, and concluded positive correlations between $\delta\nu_{\rm m}$ and g or $T_{\rm eff}$. Houdek et al. (2019, Fig. 5) studied the "modal-effect", which accounts for the coupling between convection and oscillation, and reported a similar correlations with their 1D time-dependent convection models. These works are qualitatively consistent with our best fitted parameters for dwarfs and subgiants (Table 1).

4 IMPROVEMENTS ON PARAMETER ESTIMATIONS

We now check whether applying our prescription introduces bias in the estimated stellar properties. In Fig. 3, we show the fractional differences of mass, radius, and age, between modelling without and with the prescription. The differences have medians fluctuating around 0, suggesting no systematic bias. We caution that the values we determined in Table 1 may not be directly applicable to other stellar models, which could have different outer boundary conditions. Hence, we suggest using Fig. 3 as a diagnostic plot to check this applicability. If the median values of the differences are not centred around 0, the surface parameters need to be fitted with the models being used.

Next, we demonstrate two major improvements by using our method. Firstly, we note that adopting the prescriptions

Table 1. Best fitted parameters of the surface correction prescriptions.

Model	Sample	a	b	c	d	a'	b'	c'	d'
Cubic	MS+SG	-5.59 ± 3.15	1.09 ± 0.37	-0.71 ± 2.57	-0.16 ± 0.97	—	—	—	—
Cubic	RGB	-3.87 ± 0.62	1.01 ± 0.04	-7.37 ± 0.37	-1.10 ± 0.08	—	—	—	—
Inverse-cubic	MS+SG	-5.27 ± 2.34	0.89 ± 0.35	1.47 ± 2.97	0.98 ± 1.50	-7.18 ± 2.61	0.98 ± 0.30	0.91 ± 2.64	0.79 ± 1.34
Inverse-cubic	RGB	-3.62 ± 0.36	1.14 ± 0.06	-10.83 ± 0.71	-1.55 ± 0.04	-4.71 ± 0.34	1.09 ± 0.04	-9.72 ± 0.48	-1.43 ± 0.03

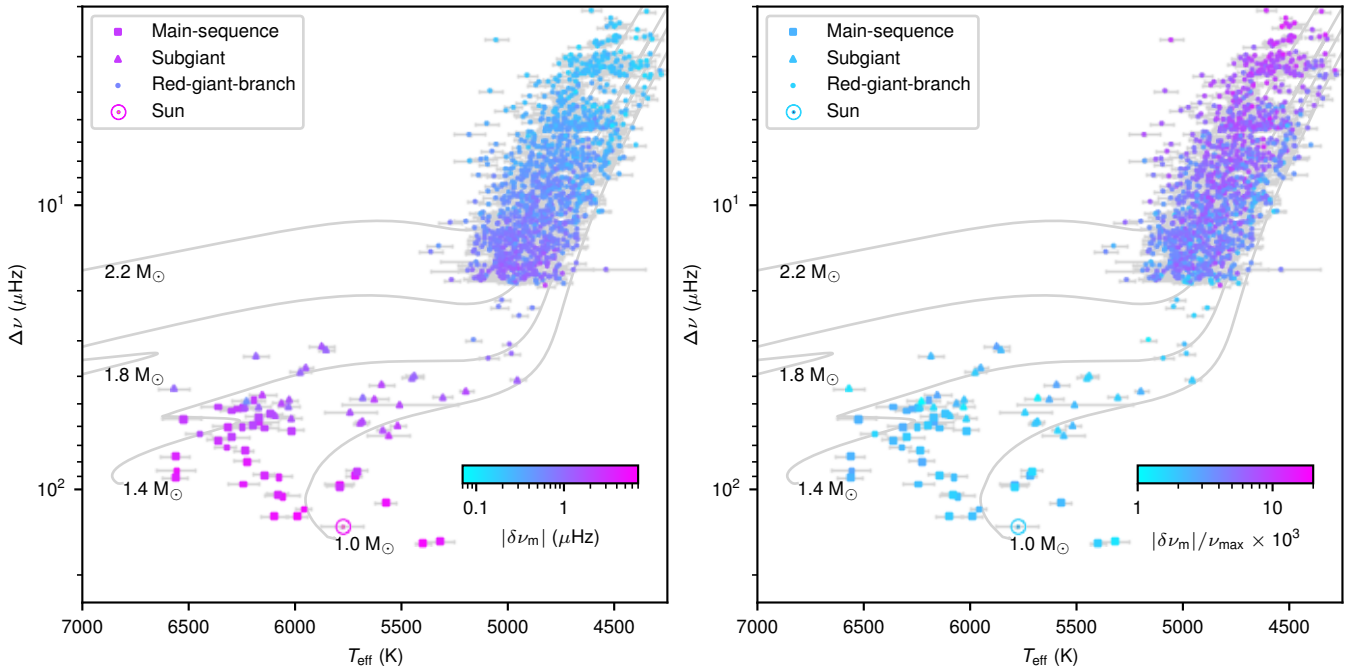

Figure 2. Surface correction at $\nu_{\rm max}$, $\delta\nu_{\rm m}$, determined based on the prescriptions with the inverse-cubic model, shown on the $\Delta\nu$–$T_{\rm eff}$ diagrams. The left panel colour-codes the absolute value of $\delta\nu_{\rm m}$ (which is negative). The right panel colour-codes the dimensionless quantity, $\delta\nu_{\rm m}/\nu_{\rm max}$. The $M = 1.0,\ 1.4,\ 1.8$ and $2.2\ {\rm M}_\odot$ evolutionary tracks are shown in grey lines.

reduces outliers when inferring parameters from stellar modelling. For example, Fig. 3 shows some stars significantly away from the median values. These data points correspond to a poor fit due to the unconstrained surface correction. To confirm this, we show the differences between the theoretical and observed values of $\Delta\nu$ in Fig. 4. The theoretical $\Delta\nu$ was determined from radial oscillation frequencies (see Appendix A for more detail). By comparing the red point in the two panels, we noticed that the differences are similar after the surface correction, independent of whether using the prescription or not. This is expected, since the corrected frequencies were constructed to fit with the observed frequencies. However, when we compare the grey points in both panels, which represent $\Delta\nu$ calculated from the uncorrected frequencies, the outliers are only present in the case of star-by-star fit (top panel). These outliers are eliminated when the prescription was applied in the ensemble fit (bottom panel).

Secondly, we argue that adopting the prescriptions also reduces scatter in model-based parameters. This can be seen from modelling stars in open clusters, members of which are expected to have the same age. We examined the test sample introduced in section 2.1, namely the RGB stars in NGC 6791 and NGC 6819. In Fig. 5, we show the probability distributions of ages for each star (in grey lines), and compare them with and without using our new prescription. It is evident that the probabilities with the prescriptions applied display smaller scatter overall. The root-mean-square values of individual model-based ages reduces to 1.41 Gyr from 1.75 Gyr for the stars in NGC 6791, and to 0.35 Gyr from 0.41 Gyr for the stars in NGC 6819.

To allow easy-access to our stellar models and the surface-corrected frequencies, we published them in an online repository (see data availability).

5 CORRECTION TO THE P-MODE LARGE SEPARATION FROM STELLAR MODELS

The scaling relation that relates the p-mode large separation $\Delta\nu$ to stellar mean density, $\Delta\nu \propto \sqrt{\rho}$ (Ulrich 1986), is broadly used (see Hekker 2020, for a review). This relation is only an approximation and stellar models have been used to correct it (White et al. 2011; Sharma et al. 2016; Guggenberger et al. 2016; Rodrigues et al. 2017; Serenelli et al. 2017; Pinsonneault et al. 2018). Sharma et al. (2016, hereafter S16) introduced a correction factor to the standard $\Delta\nu$ scaling relation:

$$\left(\frac{\Delta\nu}{\Delta\nu_\odot}\right) = f_{\Delta\nu}\left(\frac{\rho}{\rho_\odot}\right)^{0.5}, \qquad (12)$$

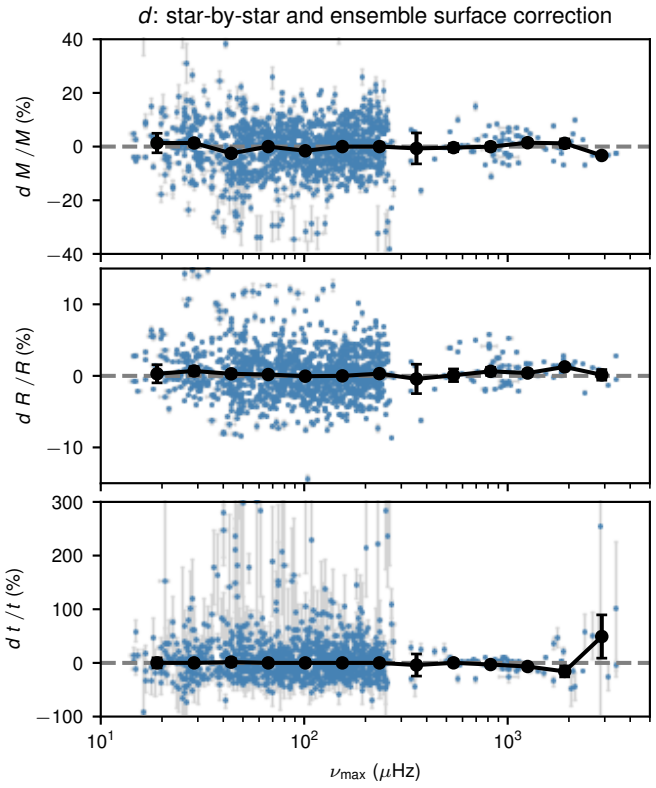

Figure 3. Fractional differences of mass, radius, and age, between modelling using star-by-star and ensemble surface correction. The medians and the associated error bars in bins of equal width in $\log \nu_{\rm max}$ are shown in black circles.

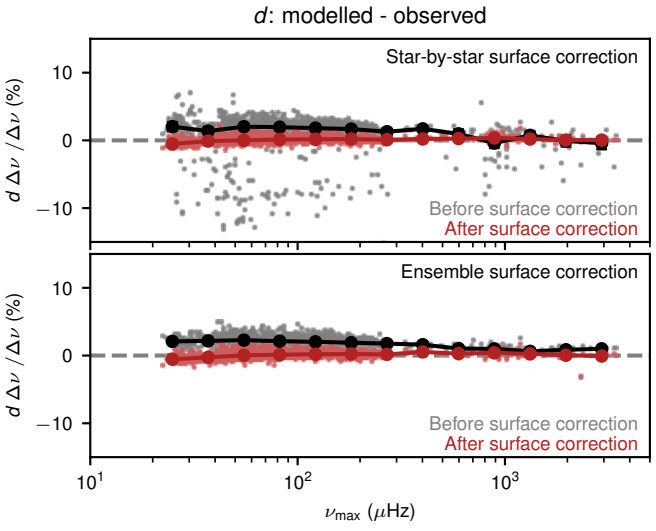

Figure 4. Fractional differences of theoretical and observational $\Delta\nu$. The top panel shows results from star-by-star fits. The bottom panel shows those from ensemble fits.

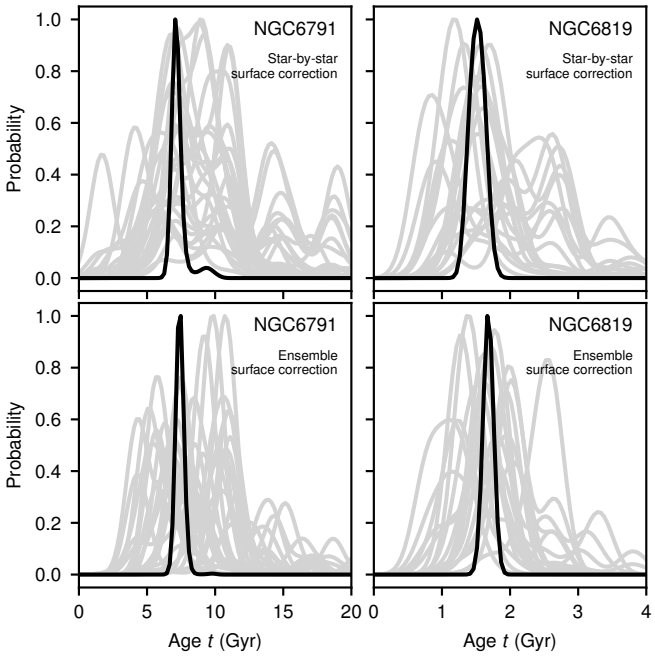

Figure 5. Probability distributions of stellar ages for the RGB stars within the *Kepler* open clusters NGC 6791 and NGC 6819. The age probability for each star are shown in grey, while the joint probability distribution is shown in black. Modelling with the prescription (lower panels) shows a reduction of the scatter in age, compared to modelling with a star-by-star surface correction (upper panels).

where $\Delta\nu_\odot = 135.1$ μHz is the solar value of the large frequency separation. In this equation, $\Delta\nu$ is usually calculated from radial oscillation frequencies. Since the surface correction is negative, we expect that the value of $\Delta\nu$ from a model will decrease when the correction is applied (Kjeldsen et al. 2008). However, this correction is usually ignored. Here, we investigate this change and analyse its implication on stellar properties derived from the asteroseismic relations.

First of all, we consider the correction factor, $f_{\Delta\nu}$, calculated from our stellar models and prescriptions. Fig. 6 shows $f_{\Delta\nu}$ as a function of $T_{\rm eff}$ (left panels) and $\Delta\nu$ (right panels), for three masses and three metallicities. The overall variations of $f_{\Delta\nu}$ resemble those calculated from models by White et al. (2011, Fig. 4) and S16 (Fig. 4), neither of which included a surface correction. However, our values for $f_{\Delta\nu}$ are systematically smaller compared to the work from S16, due to this correction. Fig. 7 shows the effect of surface correction on $f_{\Delta\nu}$. The change of $f_{\Delta\nu}$ is small for main-sequence stars, but is larger on the RGB, showing an $\sim$2% reduction, where the surface correction is relatively significant (see also Fig. 2b).

The correction factor $f_{\Delta\nu}$ are used when estimating the mass and radius via the usual scaling relations (Stello et al. 2008; Kallinger et al. 2010):

$$\frac{M}{\rm M_\odot} \approx \left(\frac{\nu_{\rm max}}{\nu_{\rm max,\odot}}\right)^3 \left(\frac{\Delta\nu}{f_{\Delta\nu}\Delta\nu_\odot}\right)^{-4} \left(\frac{T_{\rm eff}}{T_{\rm eff,\odot}}\right)^{3/2}, \quad (13)$$

and

$$\frac{R}{\rm R_\odot} \approx \left(\frac{\nu_{\rm max}}{\nu_{\rm max,\odot}}\right) \left(\frac{\Delta\nu}{f_{\Delta\nu}\Delta\nu_\odot}\right)^{-2} \left(\frac{T_{\rm eff}}{T_{\rm eff,\odot}}\right)^{1/2}. \quad (14)$$

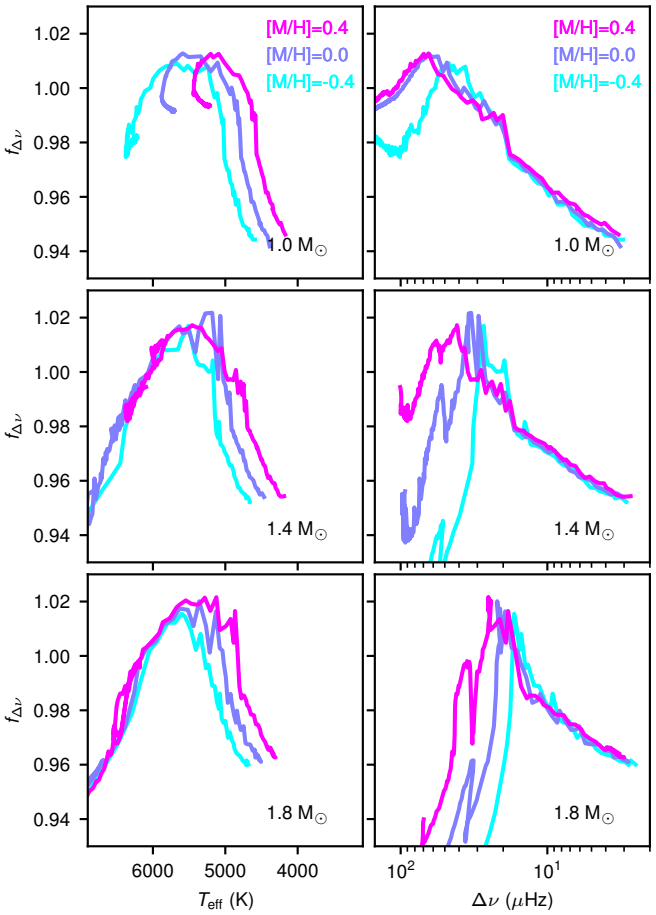

Figure 6. Correction factor for the $\Delta\nu$ scaling relation, $f_{\Delta\nu}$, as a function of $T_{\rm eff}$ (left panels) and $\Delta\nu$ (right panels) for three metallicities and three masses. The values for $f_{\Delta\nu}$ were derived using stellar models with the surface correction considered. The small fluctuations along the lines arise from the uncertainty in the helium abundance and the mixing length parameter.

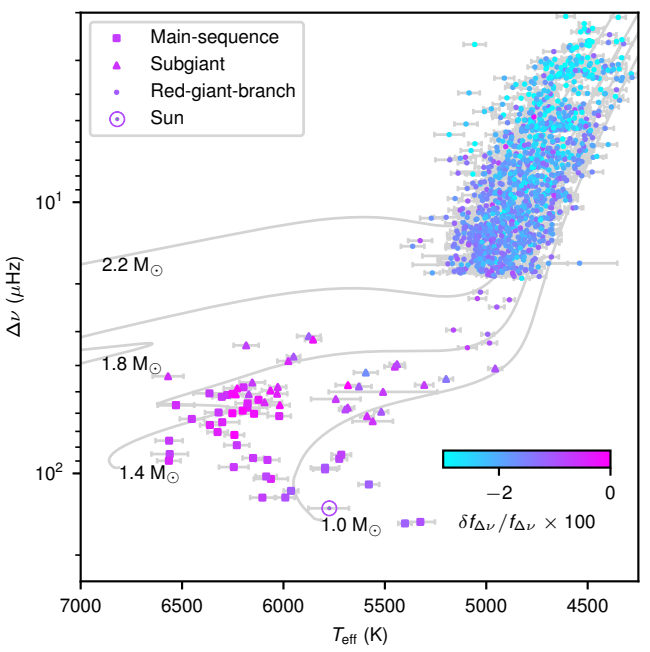

Figure 7. Fractional differences of $f_{\Delta\nu}$ between before and after the surface correction.

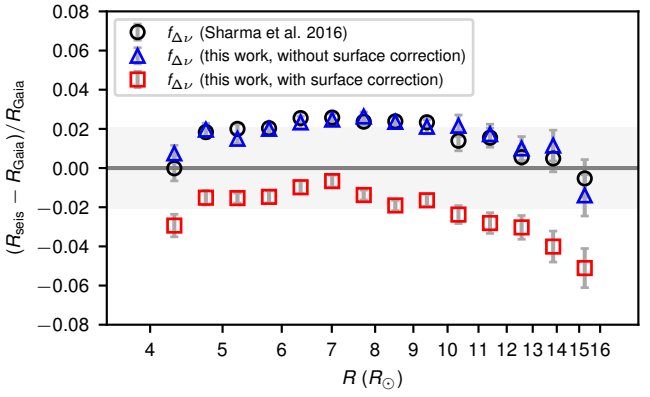

Figure 8. Comparison of *Gaia* radii and asteroseismic radii, using $f_{\Delta\nu}$ calculated in S16 and this work. The data points are binned medians, and the error bars represent the standard errors of the medians. The grey band highlights the 2% systematic uncertainties (e.g. temperature scale) presented by the analysis in Zinn et al. (2019).

To show how this change of $f_{\Delta\nu}$ affects stellar radii, we compared the asteroseismic radii with the Gaia radii calculated by Zinn (2021), using the APOKASC sample (Pinsonneault et al. 2018). The $T_{\rm eff}$ and [M/H] from APOGEE (Abdurro'uf et al. 2022) were used to derive *Gaia* radii for bolometric corrections and converting from luminosities. We calculated the asteroseismic radii through Eq. 14, where we adopted the SYD pipeline values for $\Delta\nu$ and $\nu_{\rm max}$ (Yu et al. 2018), and $T_{\rm eff}$ from APOGEE. Fig. 8 shows this comparison. Without the surface correction considered, the $f_{\Delta\nu}$ in this work (blue points) produce similar radii to S16 (black points), despite the fact that the underlying stellar models are different. In a similar experiment, Christensen-Dalsgaard et al. (2020) reported a spread of only 0.2% in the values of $f_{\Delta\nu}$ from different stellar modelling codes. A larger discrepancy emerges when we applied the surface correction (red points). Eq. 14 indicates that the seismic radius is proportional to $f_{\Delta\nu}^2$. Since correctly accounting for the surface effect reduces $f_{\Delta\nu}$ by $\sim$2% for RGB stars (Fig. 7), this translates to a systematic $\sim$4% decrease of the asteroseismic radius scale. This is exactly what we see in Fig. 8. As summarised by Zinn et al. (2019), the systematic uncertainties involved in this comparison, such as uncertainties in bolometric correction and extinction, the IRFM temperature scale, and asteroseismic reference points, can add up to 2%. It is not yet possible to conclude any disagreement between the asteroseismic and Gaia radii with this precision.

Alternatively, we can compare the asteroseismic radius and mass with the dynamical properties determined from eclipsing binaries. We used the eclipsing binary sample studied by Gaulme et al. (2016), Themeßl et al. (2018), Brogaard et al. (2018) and Benbakoura et al. (2021), who determined the dynamical masses and radii through radial-velocity and lightcurve modelling. We calculated their asteroseismic radii

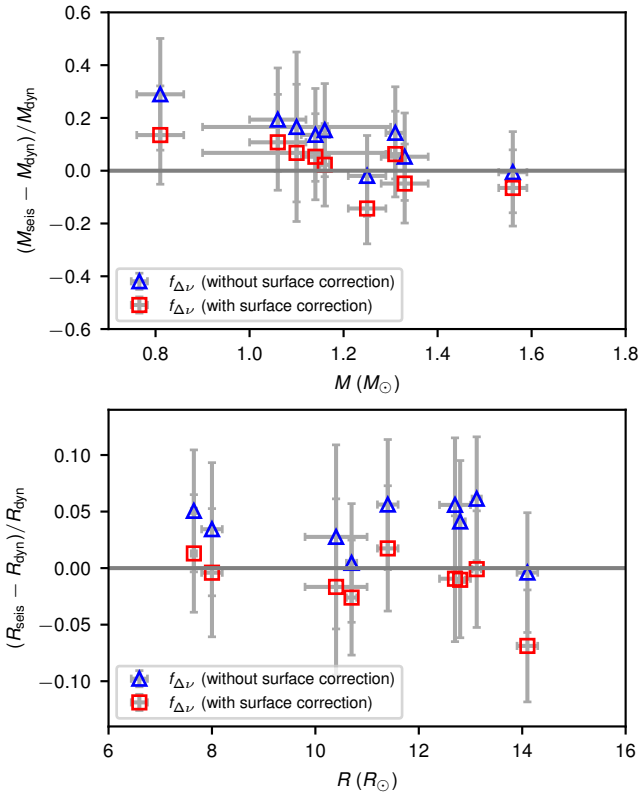

Figure 9. Comparison of the dynamical and the asteroseismic masses and radii using eclipsing binaries (Benbakoura et al. 2021). The asteroseismic properties were determined using $f_{\Delta\nu}$ with and without the surface correction, respectively.

and masses through Eq. 13 and 14, using $\Delta\nu$, $\nu_{\rm max}$, and $T_{\rm eff}$ reported in Benbakoura et al. (2021). Fig. 9 shows the resulting comparison. Using the corrected $f_{\Delta\nu}$ produces excellent agreement of those properties determined from the two independent means, while the $f_{\Delta\nu}$ without correction tends to systematically overestimate them. Benbakoura et al. (2021) also concluded the consistency between the asteroseismic and dynamical properties. Although they did not consider the surface correction in $f_{\Delta\nu}$, they modified the solar reference values appeared in the scaling relations to achieve a similar effect. Our results thus remove the need to shift the reference values (or modify the $\nu_{\rm max}$ scaling relation) when the surface correction is carefully considered.

According to Eq. 13, the scaling mass is proportional to $f_{\Delta\nu}^4$(e.g. Sharma et al. 2016). Hence, as a result of the change in $f_{\Delta\nu}$, the seismic mass scale decreases by ∼8%. This could have significant consequences for Galactic archaeology, since the ages of low-mass stars are critically dependent on their masses.

Finally, based on the observational sample and the models in this work, we can provide a simple fitting formula of $f_{\Delta\nu}$ with respect to stellar properties. We explored various functional forms (linear, log-linear and polynomial) and included the observed $\nu_{\rm max}$, $\Delta\nu$, $T_{\rm eff}$ and [M/H] as independent variables to perform simple regressions. The following form obtains a reasonably good fit ($r^2 = 0.85$) and avoids overfitting with higher orders (examined via cross-validation):

$$\begin{aligned} f_{\Delta\nu} = {} & \beta_0 + \beta_1 \log_{10}(\nu_{\rm max}/3090\ \mu{\rm Hz}) \\ & + \beta_2 \log_{10}(\Delta\nu/135.1\ \mu{\rm Hz}) \\ & + \beta_3 (T_{\rm eff}/5777\ {\rm K}) \\ & + \beta_4 (T_{\rm eff}/5777\ {\rm K})^2 \\ & + \beta_5 (T_{\rm eff}/5777\ {\rm K})^3 \\ & + \beta_6 [{\rm M/H}], \\ & {\rm for}\ 0.8 < M/{\rm M}_\odot < 2.2,\ -0.8 < [{\rm M/H}] < 0.5, \\ & {\rm and\ pre\text{-}RGB\ tip}\ (\Delta\nu > 2.0\ \mu{\rm Hz}). \end{aligned} \tag{15}$$

The best fitted parameters are $\beta = \{4.1027, 0.1706, -0.1863, -10.5526, 11.8359, -4.3733, 0.0015\}$. The generalisation to other parameter ranges, such as metal-poor, high-mass, and red-clump stars, requires more data and will be the subject of future work. Additionally, we provide a PYTHON program to derive $f_{\Delta\nu}$ given user-specified observables, from the models calibrated in this work (instead of the simple fitting formula Eq. 15). The program assigns each model with a χ^2 (using Eq. 7) and estimates $f_{\Delta\nu}$ by averaging the models weighted by $\exp(-\chi^2/2)$. For a given star of interest, the correction factor $f_{\Delta\nu}$ can then be used when estimating the mass and radius via Eq. 13 and 14.

6 CONCLUSIONS

We provide a simple prescription for the surface correction as a function of stellar properties, exploiting the fact that the correction should vary smoothly across the H–R diagram. Our main findings are summarised as follows:

(i) The absolute values of the surface correction are larger in main-sequence stars and smaller in RGB stars. For the relative surface correction as a fraction of $\nu_{\rm max}$, the trend is reversed (Fig. 2).

(ii) Using the prescription, we were able to reduce scatter and the number of outliers in stellar properties estimated from stellar modelling (Fig. 4 and 5). This demonstrates the power of our ensemble-based parameterization of the surface correction.

(iii) We present our stellar models in an online repository. The models include radial frequencies before and after applying the surface correction calibrated in this work.

(iv) Taking into account the surface correction, we revised the correction factor of the $\Delta\nu$ scaling relation, $f_{\Delta\nu}$ (Fig. 6). We provided a simpler fitting formula (Eq. 15) and a more comprehensive PYTHON program to determine $f_{\Delta\nu}$ given user-specified observables.

(v) We found that the values for $f_{\Delta\nu}$ are smaller by up to 2%, compared to those without the surface correction (Fig. 7). This results in decreases of up to 4% in radii and up to 8% in masses when using the asteroseismic scaling relations.

(vi) We showed that the mass and radius determined with the revised $f_{\Delta\nu}$ improve the agreement with those determined from eclipsing binaries (Fig. 9).

ACKNOWLEDGEMENTS

We thank Warrick Ball, Sarbani Basu, Jørgen Christensen-Dalsgaard, and Günter Houdek for interesting comments and fruitful discussions. T.R.B and D.H. acknowledge funding from the Australian Research Council (Discovery Project DP210103119). D.H. also acknowledges support from the Alfred P. Sloan Foundation and the National Aeronautics and Space Administration (80NSSC19K0597). M.J. acknowledges the Lasker Fellowship granted by the Space Telescope Science Institute. T.L. acknowledges the Joint Research Fund in Astronomy (U2031203) under cooperative agreement between the National Natural Science Foundation of China (NSFC) and Chinese Academy of Sciences (CAS) and the NSFC grants 12090040 and 12090042.

We gratefully acknowledge the Kepler teams, whose efforts made these results possible. Funding for the Kepler mission is provided by the NASA Science Mission Directorate. This paper includes data collected by the Kepler mission and obtained from the MAST data archive at the Space Telescope Science Institute (STScI). STScI is operated by the Association of Universities for Research in Astronomy, Inc., under NASA contract NAS 5–26555.

This work presents results from the European Space Agency (ESA) space mission Gaia. Gaia data are being processed by the Gaia Data Processing and Analysis Consortium (DPAC). Funding for the DPAC is provided by national institutions, in particular the institutions participating in the Gaia MultiLateral Agreement (MLA). The Gaia mission website is https://www.cosmos.esa.int/gaia. The Gaia archive website is https://archives.esac.esa.int/gaia.

Funding for the Sloan Digital Sky Survey IV has been provided by the Alfred P. Sloan Foundation, the U.S. Department of Energy Office of Science, and the Participating Institutions.

We acknowledge the use of the National Computational Infrastructure (NCI) which is supported by the Australian Government, and accessed through the Sydney Informatics Hub HPC Allocation Scheme, which is supported by the Deputy Vice-Chancellor (Research), University of Sydney.

This work is made possible by the following open-source software: Numpy (van der Walt et al. 2011), Scipy (Virtanen et al. 2020), Matplotlib (Hunter 2007), Corner (Foreman-Mackey 2016), Astropy (Astropy Collaboration et al. 2013, 2018), Pandas (Wes McKinney 2010), MESA (Paxton et al. 2011, 2013, 2015, 2018, 2019), GYRE (Townsend & Teitler 2013), PTMCMCSampler (Ellis & van Haasteren 2017), ISOCLASSIFY (Huber et al. 2017; Berger et al. 2020).

DATA AVAILABILITY

The code and processed data used in this work are available on Github.[1] The calibrated stellar models including oscillation frequencies and the correction factors $f_{\Delta\nu}$ can be downloaded from zenodo.[2] All raw data (e.g. the Keck spectra) are available on request to the corresponding authors.

[1] Github link for the code repository (replaced after publication).
[2] Zenodo link for the calibrated stellar models (replaced after publication).

REFERENCES

Abdurro'uf et al., 2022, ApJS, 259, 35
Aguirre Børsen-Koch V., et al., 2022, MNRAS, 509, 4344
Ahumada R., et al., 2020, ApJS, 249, 3
Asplund M., Grevesse N., Sauval A. J., Scott P., 2009, ARA&A, 47, 481
Astropy Collaboration et al., 2013, A&A, 558, A33
Astropy Collaboration et al., 2018, AJ, 156, 123
Ball W. H., Gizon L., 2014, A&A, 568, A123
Ball W. H., Gizon L., 2017, A&A, 600, A128
Balmforth N. J., 1992, MNRAS, 255, 632
Basu S., et al., 2011, ApJ, 729, L10
Belkacem K., Kupka F., Philidet J., Samadi R., 2021, A&A, 646, L5
Bellinger E. P., Angelou G. C., Hekker S., Basu S., Ball W. H., Guggenberger E., 2016, ApJ, 830, 31
Benbakoura M., et al., 2021, arXiv e-prints, p. arXiv:2101.05351
Berger T. A., Huber D., van Saders J. L., Gaidos E., Tayar J., Kraus A. L., 2020, AJ, 159, 280
Brogaard K., et al., 2018, MNRAS, 476, 3729
Brogaard K., Arentoft T., Jessen-Hansen J., Miglio A., 2021, MNRAS, 507, 496
Broomhall A. M., Chaplin W. J., Davies G. R., Elsworth Y., Fletcher S. T., Hale S. J., Miller B., New R., 2009, MNRAS, 396, L100
Brown T. M., Gilliland R. L., Noyes R. W., Ramsey L. W., 1991, ApJ, 368, 599
Buchler J. R., Yueh W. R., 1976, ApJ, 210, 440
Casagrande L., et al., 2021, MNRAS, 507, 2684
Cassisi S., Potekhin A. Y., Pietrinferni A., Catelan M., Salaris M., 2007, ApJ, 661, 1094
Choi J., Dotter A., Conroy C., Cantiello M., Paxton B., Johnson B. D., 2016, ApJ, 823, 102
Christensen-Dalsgaard J., 2012, Astronomische Nachrichten, 333, 914
Christensen-Dalsgaard J., Dappen W., Lebreton Y., 1988, Nature, 336, 634
Christensen-Dalsgaard J., Thompson M. J., Gough D. O., 1989, MNRAS, 238, 481
Christensen-Dalsgaard J., et al., 2020, A&A, 635, A165
Claret A., Torres G., 2018, ApJ, 859, 100
Compton D. L., Bedding T. R., Ball W. H., Stello D., Huber D., White T. R., Kjeldsen H., 2018, MNRAS, 479, 4416
Corsaro E., et al., 2012, ApJ, 757, 190
Duan R. M., Zong W., Fu J. N., Chen Y. H., Hermes J. J., Vanderbosch Z. P., Ma X. Y., Charpinet S., 2021, ApJ, 922, 2
Dziembowski W. A., Paterno L., Ventura R., 1988, A&A, 200, 213
Eddington A. S., 1926, The Internal Constitution of the Stars. The University Press
El-Badry K., Rix H.-W., Heintz T. M., 2021, MNRAS, 506, 2269
Ellis J., van Haasteren R., 2017, jellis18/PTMCMCSampler: Official Release, doi:10.5281/zenodo.1037579, https://doi.org/10.5281/zenodo.1037579
Ferguson J. W., Alexander D. R., Allard F., Barman T., Bodnarik J. G., Hauschildt P. H., Heffner-Wong A., Tamanai A., 2005, ApJ, 623, 585
Foreman-Mackey D., 2016, The Journal of Open Source Software, 24
Gaia Collaboration et al., 2016, A&A, 595, A1
Gaia Collaboration et al., 2021, A&A, 649, A1
Gaulme P., et al., 2016, ApJ, 832, 121
Gough D. O., 1990, Comments on Helioseismic Inference. Springer-Verlag Berlin Heidelberg, p. 283, doi:10.1007/3-540-53091-6
Green G. M., Schlafly E., Zucker C., Speagle J. S., Finkbeiner D., 2019, ApJ, 887, 93
Grigahcène A., Dupret M. A., Sousa S. G., Monteiro M. J. P. F. G., Garrido R., Scuflaire R., Gabriel M., 2012, MNRAS, 422, L43

Grundahl F., et al., 2017, ApJ, 836, 142
Guggenberger E., Hekker S., Basu S., Bellinger E., 2016, MNRAS, 460, 4277
Handberg R., Brogaard K., Miglio A., Bossini D., Elsworth Y., Slumstrup D., Davies G. R., Chaplin W. J., 2017, MNRAS, 472, 979
Hekker S., 2020, Frontiers in Astronomy and Space Sciences, 7, 3
Henyey L., Vardya M. S., Bodenheimer P., 1965, ApJ, 142, 841
Herwig F., 2000, A&A, 360, 952
Houdek G., Trampedach R., Aarslev M. J., Christensen-Dalsgaard J., 2017, MNRAS, 464, L124
Houdek G., Lund M. N., Trampedach R., Christensen-Dalsgaard J., Handberg R., Appourchaux T., 2019, MNRAS, 487, 595
Howard A. W., et al., 2010, ApJ, 721, 1467
Huber D., et al., 2017, ApJ, 844, 102
Hunter J. D., 2007, Computing in Science & Engineering, 9, 90
Iglesias C. A., Rogers F. J., 1993, ApJ, 412, 752
Iglesias C. A., Rogers F. J., 1996, ApJ, 464, 943
Jiang C., Gizon L., 2021, Research in Astronomy and Astrophysics, 21, 226
Johnson J. A., et al., 2017, AJ, 154, 108
Jørgensen A. C. S., Weiss A., Mosumgaard J. R., Silva Aguirre V., Sahlholdt C. L., 2017, MNRAS, 472, 3264
Jørgensen A. C. S., Mosumgaard J. R., Weiss A., Silva Aguirre V., Christensen-Dalsgaard J., 2018, MNRAS, 481, L35
Jørgensen A. C. S., Weiss A., Angelou G., Silva Aguirre V., 2019, MNRAS, 484, 5551
Jørgensen A. C. S., et al., 2020, MNRAS, 495, 4965
Joyce M., Chaboyer B., 2018, ApJ, 856, 10
Kallinger T., et al., 2010, A&A, 509, A77
Kim K.-B., Chang H.-Y., 2021, New Astron., 84, 101522
Kjeldsen H., Bedding T. R., 1995, A&A, 293, 87
Kjeldsen H., Bedding T. R., Christensen-Dalsgaard J., 2008, ApJ, 683, L175
Li Y., Bedding T. R., Li T., Bi S., Stello D., Zhou Y., White T. R., 2020a, MNRAS, 495, 2363
Li T., Bedding T. R., Christensen-Dalsgaard J., Stello D., Li Y., Keen M. A., 2020b, MNRAS, 495, 3431
Li Y., Zhang Q.-s., Wu T., Su J., Chen X.-h., Lin G.-f., Guo J.-h., Liu J.-y., 2021, ApJ, 916, 107
Li T., Li Y., Bi S., Bedding T. R., Davies G., Du M., 2022, ApJ, 927, 167
Lindegren L., et al., 2021, A&A, 649, A4
Lund M. N., et al., 2017, ApJ, 835, 172
Magic Z., Weiss A., 2016, A&A, 592, A24
Maíz Apellániz J., Pantaleoni González M., Barbá R. H., 2021, A&A, 649, A13
Manchon L., Belkacem K., Samadi R., Sonoi T., Marques J. P. C., Ludwig H. G., Caffau E., 2018, A&A, 620, A107
McKeever J. M., Basu S., Corsaro E., 2019, ApJ, 874, 180
Mosumgaard J. R., Jørgensen A. C. S., Weiss A., Silva Aguirre V., Christensen-Dalsgaard J., 2020, MNRAS, 491, 1160
Nsamba B., Campante T. L., Monteiro M. J. P. F. G., Cunha M. S., Rendle B. M., Reese D. R., Verma K., 2018, MNRAS, 477, 5052
Ong J. M. J., Basu S., Roxburgh I. W., 2021a, ApJ, 920, 8
Ong J. M. J., Basu S., Lund M. N., Bieryla A., Viani L. S., Latham D. W., 2021b, ApJ, 922, 18
Paxton B., Bildsten L., Dotter A., Herwig F., Lesaffre P., Timmes F., 2011, ApJS, 192, 3
Paxton B., et al., 2013, ApJS, 208, 4
Paxton B., et al., 2015, ApJS, 220, 15
Paxton B., et al., 2018, ApJS, 234, 34
Paxton B., et al., 2019, ApJS, 243, 10
Petigura E. A., 2015, PhD thesis, University of California, Berkeley
Petigura E. A., et al., 2017, AJ, 154, 107
Philidet J., Belkacem K., Goupil M. J., 2021, A&A, 656, A95
Pinsonneault M. H., et al., 2018, ApJS, 239, 32
Pols O. R., Tout C. A., Eggleton P. P., Han Z., 1995, MNRAS, 274, 964
Potekhin A. Y., Chabrier G., 2010, Contributions to Plasma Physics, 50, 82
Rodrigues T. S., et al., 2017, MNRAS, 467, 1433
Rogers F. J., Nayfonov A., 2002, ApJ, 576, 1064
Rosenthal C. S., Christensen-Dalsgaard J., Nordlund Å., Stein R. F., Trampedach R., 1999, A&A, 351, 689
Roxburgh I. W., 2016, A&A, 585, A63
Saumon D., Chabrier G., van Horn H. M., 1995, ApJS, 99, 713
Schmitt J. R., Basu S., 2015, ApJ, 808, 123
Serenelli A., et al., 2017, ApJS, 233, 23
Sharma S., Stello D., Bland-Hawthorn J., Huber D., Bedding T. R., 2016, ApJ, 822, 15
Silva Aguirre V., et al., 2015, MNRAS, 452, 2127
Sonoi T., Samadi R., Belkacem K., Ludwig H. G., Caffau E., Mosser B., 2015, A&A, 583, A112
Stello D., Bruntt H., Preston H., Buzasi D., 2008, ApJ, 674, L53
Stello D., et al., 2010, ApJ, 713, L182
Tayar J., et al., 2017, ApJ, 840, 17
Themeßl N., et al., 2018, MNRAS, 478, 4669
Timmes F. X., Swesty F. D., 2000, ApJS, 126, 501
Townsend R. H. D., Teitler S. A., 2013, MNRAS, 435, 3406
Trampedach R., Aarslev M. J., Houdek G., Collet R., Christensen-Dalsgaard J., Stein R. F., Asplund M., 2017, MNRAS, 466, L43
Ulrich R. K., 1986, ApJ, 306, L37
Valle G., Dell'Omodarme M., Prada Moroni P. G., Degl'Innocenti S., 2015, A&A, 579, A59
Virtanen P., et al., 2020, Nature Methods, 17, 261
Vogt S. S., et al., 1994, in Crawford D. L., Craine E. R., eds, Society of Photo-Optical Instrumentation Engineers (SPIE) Conference Series Vol. 2198, Instrumentation in Astronomy VIII. p. 362, doi:10.1117/12.176725
Wes McKinney 2010, in Stéfan van der Walt Jarrod Millman eds, Proceedings of the 9th Python in Science Conference. pp 56 – 61, doi:10.25080/Majora-92bf1922-00a
White T. R., Bedding T. R., Stello D., Christensen-Dalsgaard J., Huber D., Kjeldsen H., 2011, ApJ, 743, 161
Yu J., Huber D., Bedding T. R., Stello D., Hon M., Murphy S. J., Khanna S., 2018, ApJS, 236, 42
Zinn J. C., 2021, AJ, 161, 214
Zinn J. C., Pinsonneault M. H., Huber D., Stello D., Stassun K., Serenelli A., 2019, ApJ, 885, 166
van der Walt S., Colbert S. C., Varoquaux G., 2011, Computing in Science Engineering, 13, 22

APPENDIX A: CALCULATION OF THE P-MODE LARGE SEPARATION FROM STELLAR MODELS

The way of calculating $\Delta\nu$ from stellar models is not unique. One common approach involves using a Gaussian envelope (centred around $\nu_{\rm max}$) to weight radial modes of different orders. The model $\Delta\nu$ is determined from the slope of a linear fit to the frequencies versus the orders, using the weight assigned. However, the width of the Gaussian envelope is not obvious since stellar models can not predict the amplitude very accurately. Here, we mitigate this problem by matching the model $\Delta\nu$ to the observed $\Delta\nu$, using the stellar sample in this work.

We parameterized the standard deviation of the Gaussian envelope as

$$\Theta/\mu\mathrm{Hz} = \gamma_1 \cdot (M/\mathrm{M}_\odot)^{\gamma_2} \cdot (R/\mathrm{R}_\odot)^{\gamma_3} \cdot (T_{\rm eff}/T_{\rm eff,\odot})^{\gamma_4}, \quad \text{(A1)}$$

where M, R, and $T_{\rm eff}$ are the properties from stellar models,

and $\gamma = \{\gamma_1, \gamma_2, \gamma_3, \gamma_4\}$ are the free parameters to be determined. The weight assigned to a radial mode with frequency ν_n is given by

$$w_n = \frac{1}{\Theta\sqrt{2\pi}} \exp\left[-\frac{(\nu_n - \nu_{\rm max})^2}{2\Theta^2}\right]. \quad \text{(A2)}$$

Next, for a stellar model, the modelled large separation, $\Delta\nu_{\rm mod}$, was determined by minimising $\sum_n w_n \cdot [\nu_n - \Delta\nu_{\rm mod}(n+\epsilon)]^2$. To obtain γ in Eq. A1, we minimised the differences between the modelled and observed $\Delta\nu$ and summed over each star i:

$$\chi^2 = \sum_i \frac{(\Delta\nu_{\rm mod} - \Delta\nu_{\rm obs})^2}{\sigma^2_{\Delta\nu_{\rm obs}}}. \quad \text{(A3)}$$

In this equation, we used the SYD pipeline reported $\Delta\nu$ and the associated uncertainties as the observational values. As a result, we obtained $\gamma = \{1057.05, 0.92, -2.78, -4.05\}$. We caution that this parameterization is pipeline-dependent and should be adjusted if $\Delta\nu$ is measured using a different method from data.

This paper has been typeset from a TEX/LATEX file prepared by the author.